Inverse modeling of multimodal conductivity distributions

Gijs M. C. M. Janssen,[1] Johan R. Valstar,[2] and Sjoerd E. A. T. M. van der Zee[3]

Received 14 June 2005; revised 24 October 2005; accepted 6 December 2005; published 14 March 2006.

[1] We present a method for the calibration of multimodal hydraulic conductivity distributions and apply this method to the particular case of confining layers with a complex geological architecture. The basis of our technique is the transformation of the original multimodal conductivity distribution to the standard normal distribution, thus fulfilling the condition of normality which is required by the used representer-based inverse algorithm (Valstar et al., 2004). Using this transformation, a calibration that starts from a homogeneous prior field is shown to radically improve the estimation of the protective properties of the confining layer compared to a unimodal approach to the calibration. The method is also used for the calibration of multimodal heterogeneous prior fields. The inevitable distortion of the original parameter covariances in the posterior fields that results from the transformation process is absorbed by an iterative postprocessing procedure, in which lithologic information obtained from the distorted calibrated fields is used to condition the generation of a new multimodal field that complies again with the original geostatistics. After transformation, this new field can be calibrated again, and this process is repeated until the newly generated field agrees with the measurement information sufficiently well. Then, the lithologic distribution of this new field is fixed, and the intrafacies conductivity distributions are calibrated. This approach is shown to preserve the original geostatistics, both of the lithology field and of the intralithology hydraulic conductivity distributions.

Citation: Janssen, G. M. C. M., J. R. Valstar, and S. E. A. T. M. van der Zee (2006), Inverse modeling of multimodal conductivity distributions, *Water Resour. Res.*, *42*, W03410, doi:10.1029/2005WR004356.

1. Introduction

[2] Many aquifers in alluvial basins all over the world are covered by confining layers, which to a large extent influence the impact of human activities on the groundwater reserves below these layers. Knowledge of the hydraulic properties of the confining layers is crucial for accurately modeling the transport of contaminants toward the underlying aquifers. Confining layers often exhibit an extremely complex and heterogeneous architecture [*Bierkens*, 1994] and cannot be well described by assuming a unimodal hydraulic conductivity (K) distribution.

[3] Whereas advanced geostatistical methods are available to generate multimodal realizations conditioned on static data (K, porosity, etc.), the literature on the integration of state measurements (head, concentrations, travel time, etc.) into the conditioning procedure is very limited for the bimodal and multimodal cases. In its simplest form, calibration of multimodal hydraulic conductivity fields is performed by regarding the spatial lithology distribution as known and fixed, thus merely calibrating the intralithology hydraulic conductivity distribution. An example of this method is given by *Hendricks Franssen and Gomez-Hernandez* [2002], who used sequential self-calibration [*Gomez-Hernandez et al.*, 1998] for the inversion of the hydraulic conductivity distributions within fracture planes, treating each fracture plane as an independent statistical population. Another example is given by *Sun et al.* [1995], who expressed the hydraulic properties (K_H, K_V) belonging to every node in their model as a function of the (known) thickness distribution of the different lithologies identified within this nodes exclusive subdomain, and the (unknown but assumed constant) hydraulic conductivity $\boldsymbol{K}$ associated with these lithologies. Thus they reduced the number of unknown parameters to the number of lithologies. In both works, however, the assumed geological structure (respectively, the fracture plane distribution and the lithofacies distribution) is conditioned on static data and not further updated using the state measurements. Therefore these approaches are, in essence, not inverting the lithology field.

[4] Considerable progress toward the true inversion of lithology fields was made by *Hu* [2000], who used the Gradual Deformation method in combination with Gaussian Truncated Simulation to invert a binary lithology field. This method updates the lithology field by linearly combining either (in the first iteration) a random initial Gaussian field or (in subsequent iterations) the updated field from the previous iteration, with a number of new and independent realizations. The contribution of every realization to the new, updated field is determined by an optimization search for the set of contribution coefficients that, after truncation of the Gaussian field, minimizes the objective function. Another application of Truncated Gaussian Simulation for

[1]Department of Soil Quality, Wageningen University, Wageningen, Netherlands.
[2]Netherlands Institute of Applied Geosciences TNO–National Geological Survey, Utrecht, Netherlands.
[3]Department of Ecohydrology, Wageningen University, Wageningen, Netherlands.

0043-1397/06/2005WR004356$09.00

the inversion of lithology fields is given by *Wen et al.* [2002], who use Sequential Self-Calibration for the calibration of the Gaussian field, through its relation with the actual conductivity field that is formed after its truncation.

[5] Truncated Gaussian Simulation, however, is not generally suitable for the inversion of lithology fields with more than two soil types, as it can only produce outcrops in which the facies are sequentially ranked [*Dowd et al.*, 2003]. An extension of the Truncated Gaussian Simulation method, the Truncated Pluri-Gaussian Simulation method [*Galli et al.*, 1994], was developed to overcome this limitation. *Hu et al.* [2001] proposed the use of Truncated Pluri-Gaussian Simulation for use in the Gradual Deformation approach for the inversion of multilithology fields. *Liu and Oliver* [2004] used the Truncated Pluri-Gaussian Truncation method in a Bayesian scheme for conditioning the lithology distribution to a time series of dynamic data.

[6] A serious drawback of the Truncated Pluri-Gaussian Simulation method, that has limited the application of it for both simulation and calibration [*Liu and Oliver*, 2004], is that the parameterization of the geostatistical model (basically the covariance and cross-variance structures of the underlying Gaussian random fields and the threshold parameters to truncate them) is very complex and quite tedious. Also, it generally involves a number of ad hoc decisions and iterative trial-and-error procedures, which make the establishment of the geostatistical model somewhat murky. Despite valuable recent progress in this area, for example by *Liu and Oliver* [2003, 2004], who introduced a method for the calibration of thresholds on lithology observations, the Truncated Pluri-Gaussian Simulation method still needs considerable improvements before it can be expected to find wide application.

[7] In this paper, we will introduce an alternative and much simpler method for the inversion of multilithology fields. Furthermore, in contrast to all contributions cited above, we will generate conditional realizations with a continuous, multimodal hydraulic conductivity distribution, instead of distributions of lithologies with constant hydraulic conductivity. We will show that the geostatistical parameterization of our methodology is straightforward, and that the misfits between the calibrated model predictions and the measurements can be reduced to the level of predefined measurement errors. Our method preserves the original geostatistics, which in this work are assumed known. Calibration of the parameters of the geostatistical model is out of the scope of this paper.

[8] In the following sections, we first give an explanation of the concepts and mathematics involved in the developed inverse methodology. Then, we apply our ideas to a 2D synthetic example of a confining layer. Using this synthetic example, we examine the applicability of our inverse procedure, especially with regard to its ability to reproduce the original geostatistics.

2. Methodology

2.1. Bayesian Framework: Parameterization by Representers

[9] The stochastic inverse algorithm that we applied is an extension of the representer method, developed recently by *Valstar* [2001]. For completeness and for a good comprehension of the present study, we will here briefly recall the essence of the method.

[10] Consider the flow equation

$$A(\alpha)h - q = 0, \tag{1}$$

where h = the vector of nodal heads, q = the vector of driving forces, and $A(\alpha)$ = the system matrix depending on the parameters α. The representer method, as described by *Valstar et al.* [2004], searches for the maximum a posteriori estimates of these parameters α given observations of h. For a steady state system, if all parameters α and measurement errors v are assumed to be multivariate Gaussian distributed with known covariances and they are not cross correlated, the maximum a posteriori estimate can be found by minimizing the following objective function:

$$J = (z - M(h))^T P_v^{-1}(z - M(h)) + (\alpha - \bar{\alpha})^T P_\alpha^{-1}(\alpha - \bar{\alpha}), \tag{2}$$

where J = the objective function value, z = the vector of measurement values, $M()$ = a linear function that interpolates the vector of model predictions at the nodal points to the location of the measurements, α = the vector of parameters, $\bar{\alpha}$ = the prior mean of the parameters, P_v = the covariance matrix of the measurement errors v, and P_α = the prior covariance of the parameters. Multiplying the flow equation (equation (1)) with two times the head adjoint vector λ and adding this to the objective function (equation (2)) yields

$$J = (z - M(h))^T P_v^{-1}(z - M(h)) + (\alpha - \bar{\alpha})^T P_\alpha^{-1}(\alpha - \bar{\alpha}) + 2\lambda^T[A(\alpha)h - q]. \tag{3}$$

The addition of the flow equation to the objective function as a constraint allows for the parameters and heads to be treated independently, which has major computational advantages.

[11] The objective function is minimized if the gradients of the objective function with respect to α, h and λ are zero. Forcing this on equation (3) yields a system of three coupled Euler-Lagrange equations (see Appendix A). The solution of this system of equations gives the set of parameters α that minimizes the objective function. In order to decouple the Euler-Lagrange equations, the parameter and state variables are expressed as an expansion in a set of basis functions (see Appendix A). Every measurement adds a term to this expansion, which consists of (1) a representer, quantifying the influence of the measurement on the estimates of the variable for which the expansion is defined, and (2) a representer coefficient, quantifying the weight given to the representer (which depends on the misfit between measurement value and measurement prediction).

[12] By inserting the representer definitions in the Euler-Lagrange equations, explicit expressions for all representers and their coefficients can be obtained (see Appendix A). The adjoint head representer, the parameter representer and the head representer are calculated, respectively, in an iterative procedure, in which the unknowns in the representer expressions are replaced by their estimates from the previous iteration. The last step in each iteration is the

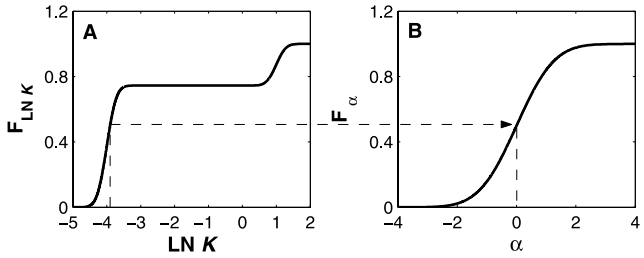

Figure 1. Illustration of the data transformation procedure from (a) F_{LNK}, the cumulative probability function of LN K, to (b) F_α, the cumulative probability function of α.

calculation of the representer coefficients, which are actually the independent parameters of the inverse model. Since there is one representer coefficient for every measurement, the number of independent unknowns is reduced to the number of measurements.

2.2. Data Transformation and Back Transformation

[13] In the unimodal case, the condition of normality of α in the Bayesian framework outlined above is usually obeyed by using the natural logarithm of K (LN(K)) for α, as previous research suggested that K values in the field exhibit a lognormal-like distribution [*Freeze*, 1975; *Hoeksema and Kitanidis*, 1985]. In the multimodal case, the condition of normality can be fulfilled by performing another, more complex transformation, relating the cumulative probability of the parameters to the cumulative probability density function (pdf) of the standard normal distribution.

[14] The multimodal lognormal distribution function of the parameter K is described by

$$p_K(K) = \sum_{i=1}^{N} \left[\frac{P_i}{K\sqrt{2\pi}\sigma_{LN(K_i)}} \exp\left(-\frac{(LN(K) - \langle LN(K_i)\rangle)^2}{2\sigma^2_{LN(K_i)}} \right) \right], \quad 0 < K < \infty, \tag{4}$$

where P_i, $\sigma_{LN(K_i)}$ and $\langle LN(K_i)\rangle$ are the marginal probability and the standard deviation and mean value of LN(K) belonging to lithology i, respectively. N is the number of lithologies.

[15] The corresponding cumulative distribution function (cdf) is then given by

$$F_K(K) = \sum_{i=1}^{N} \left[\int_0^K \frac{P_i}{K\sqrt{2\pi}\sigma_{LN(K_i)}} \exp\left(-\frac{(LN(K) - \langle LN(K_i)\rangle)^2}{2\sigma^2_{LN(K_i)}} \right) dK \right] = -\sum_{i=1}^{N} \left[\frac{1}{2} P_i erfc\left(\frac{LN(K) - \langle LN(K_i)\rangle}{\sigma_{LN(K_i)}\sqrt{2}} \right) \right] + 1 \tag{5}$$

where *erfc* is the complementary error function. The Gaussian deviate of K, denoted α, can then be found by equating the cumulative probability of K with the cumulative probability of the cdf of the standard normal distribution:

$$F_\alpha(\alpha) = \frac{1 + erf\left(\frac{\alpha}{\sqrt{2}}\right)}{2}, \tag{6}$$

where *erf* is the error function.

[16] As $F_K(K)$ is known from equation (5), α can be calculated using the inverse of the cumulative standard normal distribution function. The transformation procedure is illustrated in Figure 1.

[17] The back transformation of α can be achieved with a hybrid Newton-Raphson/Bisection root finding algorithm [*Press et al.*, 1986] to look for the value of K that equates equation (5) with equation (6) (with an accuracy of at least 10^{-6}). The derivative of K with respect to α, needed for the Newton-Raphson algorithm and also for the evaluation equations (A9)–(A11), is given by

$$\frac{dK}{d\alpha} = \frac{p_\alpha(\alpha)}{p_K(K)}. \tag{7}$$

2.3. Prior Fields

[18] In this paper two different types of calibration are performed: calibration starting from a homogeneous prior field and Monte Carlo calibration of heterogeneous prior fields. In our case of multimodal conductivity distributions both require a very different approach.

[19] Calibration starting from homogeneous prior fields can serve, for example, as a quick assessment of system response (conditional to the available measurements), the systems posterior covariances of the parameters and states, and its sensitivities [*Valstar*, 2001; *Valstar et al.*, 2004]. Only one realization has to be calibrated, and therefore this approach has preference over (usually) time-consuming Monte Carlo runs. The representer method allows for the calculation of the posterior parameter and state variances by applying a linearization around the last estimates [*Valstar*, 2001; *Valstar et al.*, 2004], and these posterior variances can be used, for instance, to guide future measurement campaigns.

[20] More challenging than the calibration of initially homogeneous fields, where reproduction of the reference geostatistics is not a prerequisite as such, is the inverse modeling of heterogeneous multimodal prior fields. This is necessary if, for example, one wants to quantify the inherent uncertainty in model predictions made with a model in which the linearization assumption is not valid. In that case, a Monte Carlo analysis has to be performed, which means that a large number of unconditional realizations that obey the reference statistics are calibrated into equiprobable realizations that still obey the reference statistics but are now also conditional to all measurements. The more (valuable) measurements are included in the calibration, the smaller the variance in model parameters and model predictions that is encountered in the Monte Carlo series.

[21] If, however, a heterogeneous, multimodal realization is calibrated with the procedure described above, the resulting calibrated realization will not obey the reference geostatistics. This is the case because the α variogram is a composite variogram constructed from $N + 1$ different covariance functions (C_I and C_i, i = 1,2 ...N). Since the variance gain over a certain lag distance can never be the exact representation of the variance gain of more than one variable, information is always lost when variograms are combined. The $N + 1$ separate variograms can therefore (after back transformation) never be reproduced when the α variogram is used for simulation. Furthermore, simulation

using the α variogram per definition induces cross correlation between the intrafacies K distributions that was originally not there.

[22] We have designed an iterative postprocessing procedure that preserves the original correlation structure of the indicator field. As the method is better explained using a specific numerical example, its details will be discussed in section 3.5.

3. Simulation

3.1. Conceptual Model

[23] We considered the synthetic example of a 2D complex confining layer of 500 (length) by 20 (depth) m, discretized into 250 $\times$ 40 elements. Thus, in the absence of any direct information on the hydraulic conductivity, the number of parameters to be estimated is 10^4. On top of the confining layer we assumed a homogeneous sandy layer of anthropogenic origin with a thickness of 3 m (discretized into 250 $\times$ 1 elements) and a known hydraulic conductivity of 3.0 m/d, and underneath the confining layer we assumed a sandy aquifer with a thickness of 10 m (discretized into 250 $\times$ 1 elements) and a known value for K of 0.6 m/d.

[24] A steady state head distribution was obtained with MODFLOW [*McDonald and Harbaugh*, 1984] by assigning recharge (250 mm/y) to the top of every top layer grid cell and by imposing constant heads of 0.0 m and 2.0 m in the utmost left and utmost right cell of the aquifer layer, respectively. A schematic representation of the flow model is given in Figure 2.

3.2. Reference Confining Layer and Reference Geostatistics

[25] The measurements with which the calibrations in this study were performed were obtained from a bimodal as well as a trimodal synthetic reference (or "true") field. These reference fields were constructed in two steps: first, an unconditional two-class (or three-class) indicator field $I(\mathbf{x})$ ($\mathbf{x}(x_1,x_2)$ is the vector of Cartesian coordinates, I = 1,2 or 3) was generated with the GSLIB program SISIM [*Deutsch and Journel*, 1998]. Then, using the GSLIB program SGSIM, an intrafacies hydraulic conductivity distribution was generated for every lithology type ($Y_i(\mathbf{x})$ = LN($K_i(\mathbf{x})$), i = 1, 2 or 3). The intrafacies K distributions were combined into one continuous bimodal or trimodal realization of $K(\mathbf{x})$ according to the indicator field ($K(\mathbf{x}) = K_i(\mathbf{x})$ if $I(\mathbf{x})$ = i). The

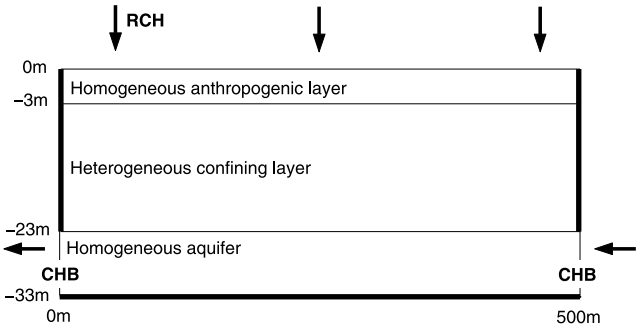

Figure 2. Schematic representation of the flow model. Heavy border lines indicate no-flow boundaries. Arrows indicate water sources and sinks. CHB is constant head boundary, and RCH is recharge.

Table 1. Geostatistics of the Unconditional Indicator Fields, Continuous Fields, and the Transformed Fields[a]

Parameter	Value
Indicator Fields	
P_1 for bimodal case	0.75
P_2 for bimodal case	0.25
$P_1 = P_2 = P_3$ for trimodal case	0.33
$a_{H,1} = a_{H,2} = a_{H,3}$, m	100.0
$a_{Z,1} = a_{Z,2} = a_{Z,3}$, m	10.0
Variogram model	Exponential
Continuous Fields	
$\langle Y_1 \rangle$ (LN), m/d	−4.0
$\langle Y_2 \rangle$ (LN), m/d	1.0
$\langle Y_3 \rangle$ (LN), m/d	−2.0
$\sigma^2_{Y_1} = \sigma^2_{Y_2} = \sigma^2_{Y_3}$	0.05
a_{H,K_1}, m	20.0
a_{Z,K_1}, m	3.5
$a_{H,K_2} = a_{H,K_3}$, m	10.0
$a_{Z,K_2} = a_{Z,K_3}$, m	3.0
Variogram model	Exponential
"Equivalent" Unimodal Fields [b]	
$\langle Y \rangle$ (LN), m/d	−2.75
σ^2_Y	4.74
Variogram model	equation (9)
Transformed Fields	
$\langle \alpha \rangle$	0.0
σ^2_α	1.0
$a_{H,\alpha}$, m bimodal/trimodal	78.01/84.00
$a_{Z,\alpha}$, m bimodal/trimodal	8.30/9.50
$w_{H,\alpha}$ bimodal/trimodal	0.67/0.83
$w_{Z,\alpha}$ bimodal/trimodal	0.73/0.78
Variogram model	equation (8)

[a] Numerical subscripts indicate lithologies. Subscript H stands for the horizontal direction and subscript Z for the vertical direction.
[b] Only given for the bimodal case.

properties of the indicator fields and the continuous intralithology distributions are given in Table 1. The reference indicator fields are shown in Figure 3.

[26] When transforming a multimodal lognormal hydraulic conductivity field into a standard normally distributed one, its original geostatistical structure will be lost. In the first place, the transformed field, being standard normally distributed, will always have a mean and sill of approximately 0.0 and 1.0, respectively. Furthermore, the horizontal (a_H) and vertical (a_Z) ranges change. Finally, also the type of variogram (the variogram model) that applies for the transformed field differs from the one for the multimodal lognormal field.

[27] To obtain the parameter covariance matrix (P_α in equation (2)) of the transformed field, 5000 unconditional, equiprobable realizations of the confining layer with the same geostatistical properties as the reference confining layer were generated. These realizations were then transformed according to the transformation procedure described above. Using a modified version of the GSLIB program GAM [*Deutsch and Journel*, 1998], the average horizontal and vertical variogram of all transformed realizations were calculated, constituting P_α.

[28] Table 1 gives the geostatistical parameters for the transformed fields as they resulted from this multirealization approach. The model to which these parameters belong is different from the original exponential model or any other well known variogram model. It appeared that for both the

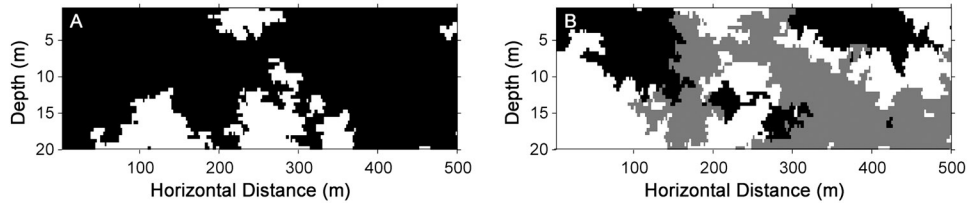

Figure 3. Reference lithology fields for the (a) bimodal and (b) trimodal cases. Black, white, and gray correspond to indicator class I = 1, 2 and 3, respectively (see Table 1 for their properties).

bimodal and the trimodal case, the variograms could be described very well with the following model:

$$\gamma(s) = c \cdot \left[1 - \exp\left(-\frac{3s^w}{a^w}\right)\right], \tag{8}$$

where γ = the variance, c = the sill, s = the lag distance, w is a constant ($w < 1$), a is the effective range and a^w is the actual range. Note that not only a but also w is different for the two principal directions.

[29] Throughout the rest of the paper, the statistics given in Table 1 for the untransformed fields will be referred to as the ''reference geostatistics''.

3.3. Measurement Sets

[30] In the reference field, 36 measurement locations were selected according to a regular grid. Different subsets of these measurement locations were used as input for the calibration procedure: we used subsets of 12, 18, 24 and 36 head measurements and equally sized subsets of K measurements. In the following, measurement sets will be referred to with a code consisting of the number of measurements of each type. For example, a measurement set with 18 head and 18 K measurements is indicated as the 18H18K measurement set. The locations sampled in the various subsets are given in Figure 4. Figure 4 holds for both head and K measurements (so a subset of K measurements consists of the same measurement locations as the equally sized subset of head measurements).

[31] Gaussian-distributed synthetic measurement errors were added to the head measurement values to account for their uncertainty: a measurement error variance of 0.001 m^2 was assumed. The method of incorporation of K measurements in the calibration procedure depended on whether a homogeneous prior field was being calibrated (section 3.4) or a heterogeneous prior field in a Monte Carlo series (section 3.5). In the first case, actual continuous K measurements were sampled from the reference field and transformed to α, and a measurement error was added to them. A measurement error standard deviation of 20 and 10 percent of the mean K value of the corresponding lithology was assumed for K measurements that fell into the low- and high-conductivity category, respectively. Note that the measurement variance P_{ij} (i = j) that has to be applied to α is dependent on the value of α. In the Monte Carlo series, only the lithology type was extracted from the reference field at the measurement locations, and this information was incorporated in the calibration procedure by conditioning the prior indicator fields on it. This point is explained further below.

[32] The measurement information, together with the reference geostatistics, was assumed to be the only prior information available about the true hydraulic conductivity field.

3.4. Calibration Starting With Homogeneous Prior Fields

[33] We performed this type of calibration only for the bimodal case. The absence of prior knowledge about the distribution of the parameter α over the domain was expressed by setting it at its mean value ($\alpha = 0.0$) everywhere. For the bimodal case, this value of α corresponds to K = 0.06 m/d. The calibration was performed with both the 36H and the 18H18K measurement set.

[34] For illustrative purposes, the calibration calculations were repeated using a unimodal approach, an approach a

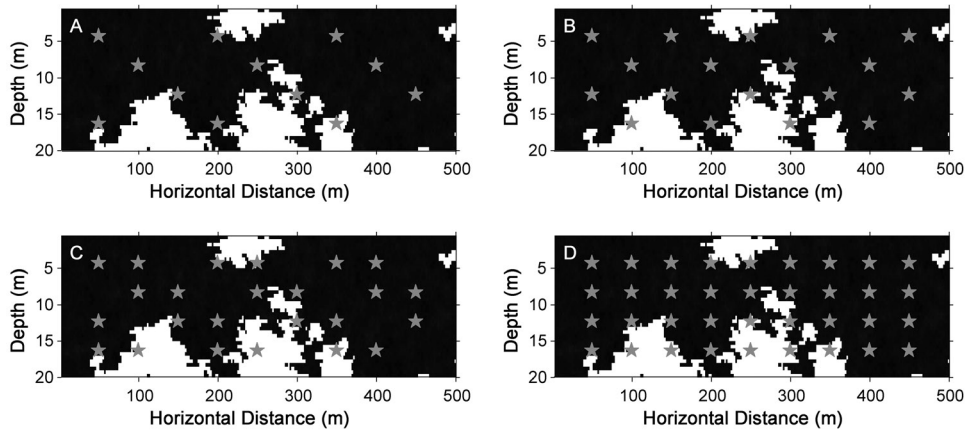

Figure 4. Configuration of the (a) 12H, (b) 18H, (c) 24H, and (d) 36H measurement sets, which are identical to the 12K, 18K, 24K, and 36K measurement sets, respectively.

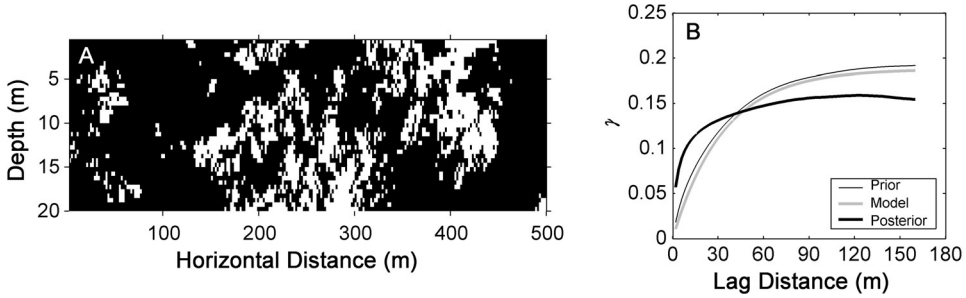

Figure 5. (a) Example of a calibrated lithology field before postprocessing and (b) the horizontal prior, theoretical, and posterior indicator variograms averaged over 100 posterior realizations (also without postprocessing).

modeler inadvertently could choose if he fails to recognize the existence of multiple statistical populations of K. The bimodal nature of K is then replaced by the normal distribution with the same overall mean and variance. The covariance function that is now needed to describe the composite geostatistical properties (see Table 1) and to fill P_α can be obtained using the analytical result presented by *Rubin* [1995], *Lu and Zhang* [2002], and *Rubin* [2003]:

$$C(s) = \left(P_1^2 + C_I(s)\right)C_1(s) + \left(P_2^2 + C_I(s)\right)C_2(s) + C_I(s) \cdot \left(\langle Y_1\rangle - \langle Y_2\rangle\right)^2, \quad (9)$$

where C_1, C_2, C_I and C are the two intrafacies covariance functions and the indicator and composite covariance functions, respectively.

3.5. Monte Carlo Calibration

[35] As stated above, the transformation procedure and therefore also the calibration procedure destroy the reference geostatistics. An example of a posterior field calibrated on the 24H measurement set, together with the average horizontal prior, theoretical and posterior indicator variograms averaged over an ensemble of 100 posterior realizations conditioned on the same measurement set, is given in Figure 5. It is clear that the integral scales of the lithology field are severely underestimated.

[36] However, the calibrated field *does* give information on where the inverse algorithm wants to decrease the amount of one lithology in favor of another. This information can be used in a postprocessing procedure that iteratively results in a conditional realization that obeys the reference geostatistics. This postprocessing procedure consists of the following steps:

[37] 1. Generate an indicator field that is conditional to the available K measurements (if any) and that obeys the reference geostatistics (with SISIM).

[38] 2. Generate unconditional K_i (i = 1,2...N) fields (with SGSIM) and combine them according to the indicator field.

[39] 3. Calculate the objective function (this objective function is discussed below).

[40] 4. Calibrate the resulting bimodal realization using the methodology described above. Note: this results in fields with distorted geostatistics, as the field shown in Figure 5a.

[41] 5. Determine which cells in the model have *not* changed lithology during the calibration.

[42] 6. Generate (with SISIM, using the reference geostatistics) a new indicator field conditioned on the cells that have *not* changed lithology and on the available K measurements (if any).

[43] 7. Repeat steps 2–6 until the objective function in step 3 meets a certain convergence criterion (this convergence criterion is discussed below).

[44] 8. Combine the resulting lithology field with the initial K_i (i = 1,2...N) fields (from the first time that step 2 was executed).

[45] 9. Calibrate the intrafacies hydraulic conductivity distribution.

[46] The objective function used in step 3 differs from the objective function used in the representer method (see Appendix A). The evaluation of the objective function used in the representer method requires the calculation of the representer expansions, which can only be done for the transformed field. Instead, we simply used a least squares objective function in step 3, summing, over all measurements, the squared differences between the measurement value and the model prediction. The value of the convergence criterion, with which the value of the objective function in step 3 is compared, was calculated as follows:

$$C_{crit} = N_{meas} \cdot V_{head} + \sum_{m=1}^{N_{meas}} \sigma^2_{head,m}, \quad (10)$$

where N_{meas} is the number of measurements, V_H is the head measurement error variance (= constant for all head measurements), and $\sigma^2_{head,m}$ is the head variance at measurement location m assuming a fully known spatial lithology distribution and a completely unknown intrafacies K distribution. Thus the first part of the right-hand side of equation (10) accounts for the measurement errors, which allow a certain deviation of the model predictions made with the calibrated realization from the measurement values. The second part of the right-hand side reflects the variance that can be resolved by calibrating the intralithology hydraulic conductivity distributions, after an appropriate lithology distribution has been found. So, this variance does not have to be resolved during the calibration of the lithology distribution. An approximate value for $\sigma^2_{head,m}$ was obtained by calculating the average squared difference between the reference head value at the measurement location and the head value at the same location in 100 realizations having the reference lithology distribution but varying K_i (i = 1,2...N) realizations.

[47] The maximum number of iterations allowed in step 4 was set at 10. Because of the high nonlinearity of the problem, it happened occasionally that convergence was not reached after 10 iterations, or that the calibration got stuck in a local minimum. However, even fields that are not fully calibrated, or fields trapped in a local minimum, contain information about necessary parameter adjustments. Therefore, in such situations, the algorithm was set to proceed as usual to step 5.

[48] In step 5, the lithology distribution has to be regained from the continuous α distribution. This was done by back transforming α to K as explained in section 2.2, and then appointing threshold values of K to distinguish between the lithologies. The threshold between two lithologies was set at the value of K (between the two mean values of the lithologies) with the lowest probability. Considering the small intrafacies variances and the high contrasts between the mean K values of the facies, the probability of assigning the wrong lithology type to a certain value of α was extremely low and did not hamper the calibration.

[49] As the number of iterations in the postprocessing procedure increases, the number of conditioning cells used in step 6 grows, thereby more and more fixing the newly generated indicator field and limiting the variation that induces progression in the convergence. This can cause the convergence to stop preliminarily. Therefore, in runs in which it was found necessary to promote the convergence speed, the new indicator field generated in step 6 was simulated with the Kriging of the unknown cells based on only a very small number of previously simulated nodes (the value of *nodmax* in SISIM was set at 2). This reduces the influence of the conditioning cells on the simulation of the unknown cells, and thus more variation is created in the simulation of these cells. We applied this technique in case both the number of iterations was larger than 10 and the objective function was still larger than 50% of its original value.

[50] In step 2, new K_i (i = 1,2. . .N) fields were generated with a randomly sampled value for the seed in every iteration. This was found necessary in order to preserve the reference lithology geostatistics, for the following reason. A cell that has not changed lithology during a certain iteration, is not likely to change lithology in upcoming iterations either if the prior intrafacies K distribution with which the calibration in step 4 starts remains the same. In other words: once a cell has been added to the conditioning file used in step 6, it is unlikely to be removed from this file in the remainder of the postprocessing procedure. Remember that the pattern of cells changing or keeping their lithology does not follow the correct variogram and so neither does the set of conditioning cells. Thus the new indicator field generated in step 6 will be increasingly distorted. If, however, the intrafacies K distribution that enters step 4 is changed in every iteration, only those cells that do not change lithology in step 4 regardless of this intrafacies K distribution, are part of the subset of permanent conditioning cells. The set of remaining conditioning cells changes from iteration to iteration and therefore its disturbing influence on the geostatistics of the newly generated indicator field in step 6 will not increase, but instead is corrected during subsequent iterations.

[51] The calibration of the intrafacies K distributions (step 9) was performed using the representer method, assuming zero correlation between cells that have a different lithology, and using the appropriate intrafacies geostatistics to calculate the covariance between cells that have the same lithology.

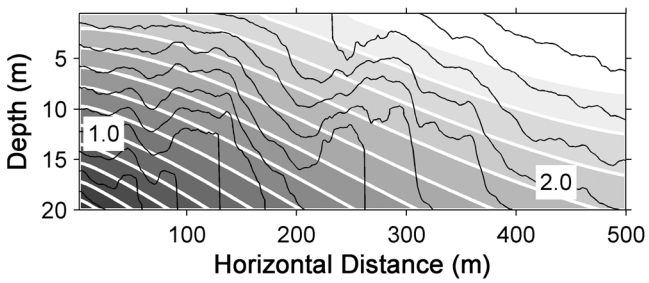

Figure 6. Comparison, for the bimodal case, between the reference head distribution (black lines) and the prior head distribution (white lines and gray scale) calculated from the homogeneous prior field.

4. Results

4.1. Calibration Starting With Homogeneous Prior Fields

[52] Figure 6 shows the reference and the prior head distribution within the confining layer. The prior field shows a regular head fall from the upper right corner of the domain to the bottom left corner, where the head was preset at 0.0 m. The reference head field, however, shows considerable deviations from this regular pattern, especially at the locations of the high-conductivity lenses which locally cause the flow to be more horizontally directed than in the prior, homogeneous field.

[53] The head and K fields calibrated on the 36H measurement set with the unimodal and the bimodal approach, are given in Figure 7. Although both calibration approaches yielded head distributions that fit the head measurements equally well, the head fields and the calibrated K fields produced by them are clearly very different in nature. In the unimodal approach, all necessary parameter adjustments to make the head field fit the measurements could be realized within the low-conductivity lithology (see Figures 7c and 7e): although the input variance $\sigma^2_{LN(K)}$ of the unimodal approach was 4.74, the posterior value of $\sigma^2_{LN(K)}$ was only 0.49. This resulted in a head field (Figure 7a) that is still rather smooth compared with the reference head field. In contrast, the bimodal calibration approach yielded a much more realistic K field (Figures 7d and 7f), with two distinct lithologies just as in the reference field. Both the unimodal and the bimodal approach predicted the high-conductivity zones at the correct locations (the locations of the high-conductivity lenses in the reference field), but only in the bimodally calibrated K field the difference between the high- and low-conductivity zones are as pronounced as in the reference field. Therefore the posterior head field of the bimodal approach (Figure 7b), although equally close to the measurement values, exhibits an overall pattern that resembles the reference head field much better than the posterior head field of the unimodal approach. Especially the horizontally directed flow at the

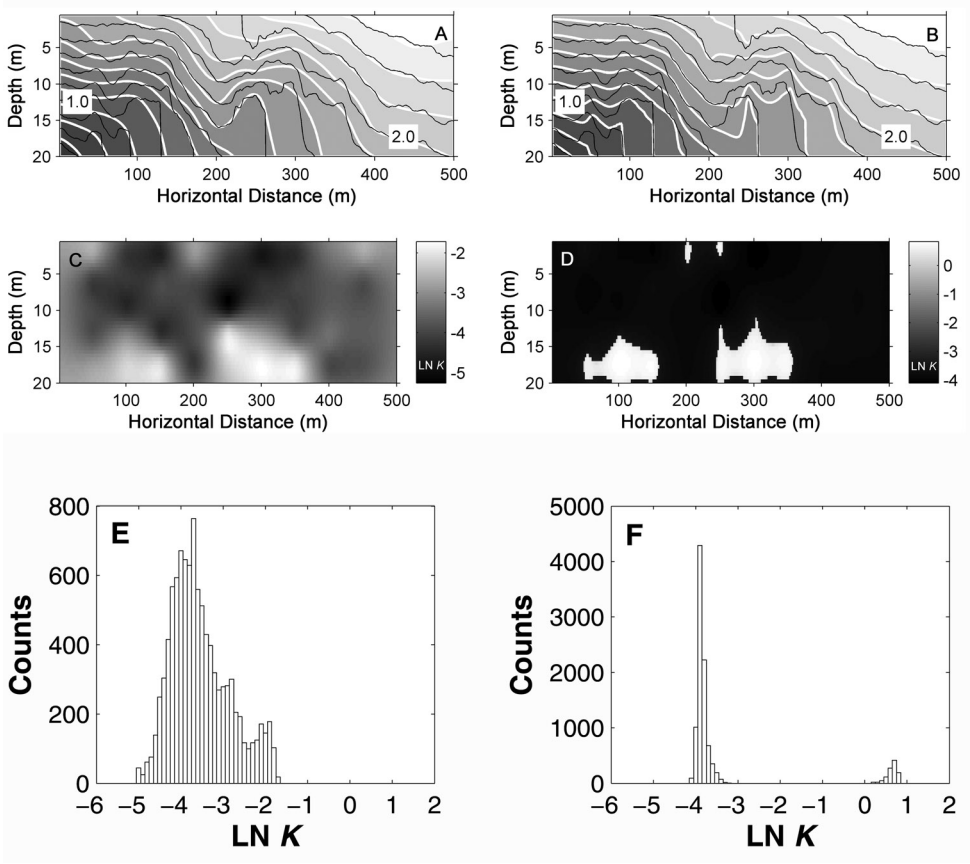

Figure 7. Calibration results obtained with (a and c) the unimodal and (b and d) the bimodal approach and (e and f) histograms of LN K values as they occur in Figures 7c and 7d, respectively. Figures 7a and 7b compare the calibrated head fields (white lines and gray scale) with the reference head distribution (black lines). Figures 7c and 7d show the calibrated LN K distributions. In Figure 7d, no intraface K variation is visible because of the large contrast in the mean conductivity of the facies.

locations of the high-conductivity lenses is much better predicted. We also obtained the conditioned travel times needed for particles released in the top cell of every column in the numerical model to reach the lower aquifer, using the particle-tracking software MODPATH [*Pollock*, 1994]. Figure 8 illustrates that the bimodal calibration results in a major improvement of the transport predictions. Also the posterior parameter and state variances and sensitivities can be expected to be much more accurate using the bimodal approach than using the unimodal approach.

4.2. Monte Carlo Simulation

[54] For the iterative postprocessing procedure outlined in section 3.5 to succeed (that is, to result in equiprobable realizations obeying the reference geostatistics and conditional to all the measurements) it is crucial that during the

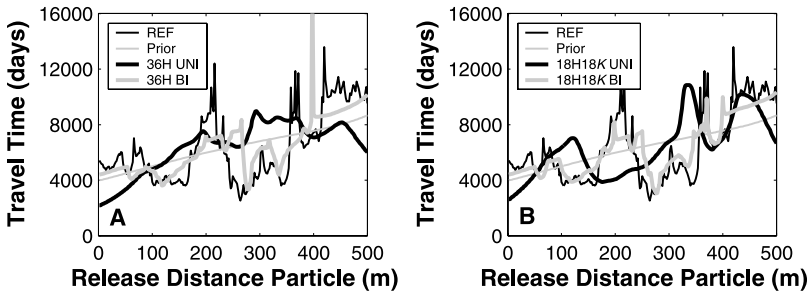

Figure 8. Unconditional ("Prior") and conditional (to (a) the 36H and (b) the 18H18K measurement set) travel times needed for particles starting from the top of the anthropogenic layer to reach the groundwater layer, compared with the reference ("REF") travel times. UNI is the unimodal approach, and BI is the bimodal approach.

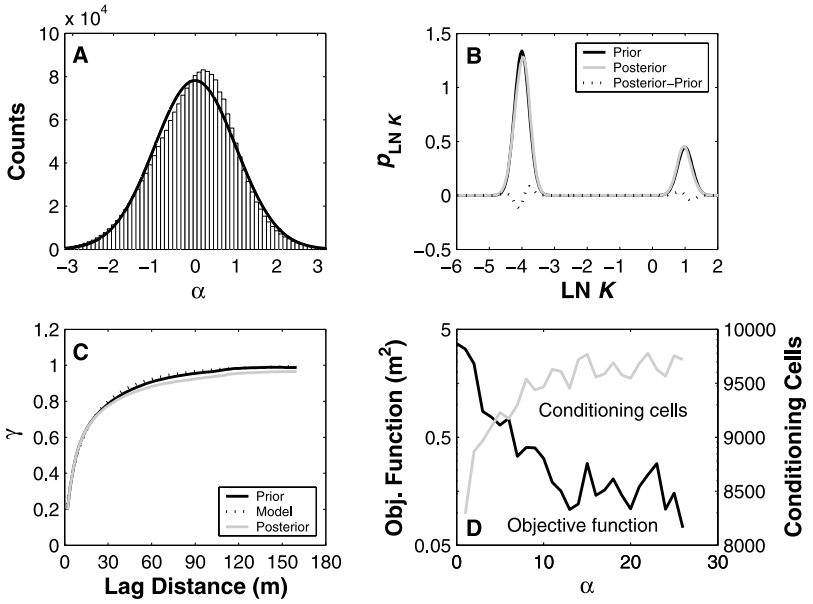

Figure 9. (a) Comparison of the posterior α histogram with the theoretical variogram as given by the standard normal distribution (black line). (b) Comparison between the prior and posterior LN K distributions. The dotted line gives the numerical difference between the two. (c) Comparison of the averaged posterior α variogram with the averaged prior and model variogram. (d) Example of the development of the objective function (logarithmic scale) during the calibration of one specific multimodal field, together with the development of the number of conditioning cells used in step 6 of the iterative postprocessing procedure.

calibration in step 4 (section 3.5) the properties of α (specifically the shape of its distribution and its variogram) are preserved. Otherwise, a bias will be introduced that will propagate through the iterative postprocessing procedure. Figure 9a shows, for the bimodal case, the α histogram of 200 realizations calibrated (without postprocessing) with the representer method, starting from random continuous bimodal fields and using the 24H measurement set. This histogram is compared to the theoretical histogram defined by the standard normal distribution. To exclude the influence of the reference field on the posterior histogram (which would result in a systematic bias), every unconditional realization from the Monte Carlo series was calibrated using measurements taken from a different reference field. Whereas the prior distribution of α matched the theoretical distribution almost perfectly (data not shown), the calibration introduces a minor bias of α toward values that are close to the lithology threshold ($\alpha = 0.675$). It is conceivable that this is due to the extremely high value of the derivative $dK/d\alpha$ at this threshold, which can trick cells into an unjustified lithology switch. In later iterations, this switch will sometimes not be completely undone anymore, but only partially by moving the α value of this cell close to the threshold value. However, after back transformation of the values with which the α histogram was constructed, this bias appears not to affect the relative proportions of the two lithologies, and it only has an insignificant effect on the shape of the intrafacies hydraulic conductivity probabilities (see Figure 9b).

[55] Except for a minor reduction of the sill variance due to the small bias discussed above, the horizontal α variogram is preserved well after calibration (see Figure 9c): the range and the model type are unaffected. The reproduction of the vertical α variogram was equally good. In summary, Figure 9 shows that the representer method is able to handle the calibration of the normal transform of a bimodal variable in a satisfactory manner, despite of the difficulties that were to be expected because of the very high value of $dK/d\alpha$ at the threshold value of α. The calibration in step 4 of the iterative postprocessing procedure will not introduce a significant bias in the lithology distribution.

[56] Figure 9d shows, for one particular initial realization in this Monte Carlo run, the development of the objective function as evaluated in step 3 of the iterative postprocessing procedure, as well as the number of conditioning cells used in step 6 to generate the next lithology field.

[57] Decisive substantiation of the iterative postprocessing procedure for the calibration of continuous multimodal fields is achieved if the average statistical properties of a sufficient number of conditional realizations are shown to be close to the reference statistics. To this aim, 100 unconditional random continuous bimodal realizations were calibrated on the 24H measurement set, again using a different reference field for every realization to be calibrated. This number of Monte Carlo calculations appeared to be enough to achieve convergence of the results (average variograms). Figure 10a shows a comparison between the horizontal indicator variogram modeled using the reference statistics (see Table 1) and the averaged prior and posterior (line "Posterior 1") horizontal indicator variogram. It shows that during calibration, the prior indicator variogram is preserved reasonably well. The small deformation of the variogram is caused by lowering *nodmax* in SISIM in slowly converging realizations (see §3.5): the average posterior variogram of the 51 (out of 100) realizations that did not require lowering *nodmax* in their calibration (line

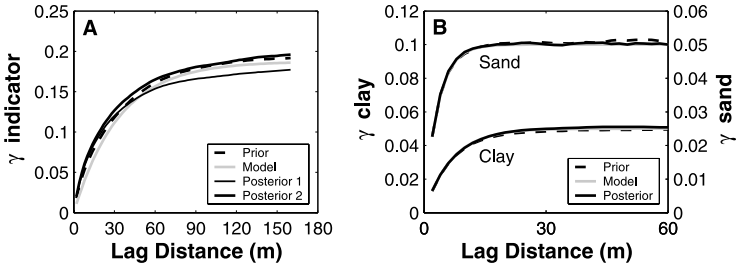

Figure 10. (a) Comparison of the posterior indicator variograms, both averaged over all posterior realizations ("Posterior 1") and averaged over only those realizations the calibration of which did not require adjustment of *nodmax* ("Posterior 2"), with the averaged prior indicator variogram and the model variogram. (b) Comparison of the averaged posterior intrafacies variogram with the averaged prior and model variogram.

"Posterior 2" in Figure 10a) resembles the prior variogram very well. Equally good results were found for the vertical indicator variogram.

[58] After the convergence criterion for the calibration of the lithology distribution was met, the intrafacies hydraulic conductivity distributions were calibrated (step 9 in §3.5). For all 100 Monte Carlo realizations, only one extra iteration was required with the representer method to fulfill the convergence criterion. Figure 10b shows that the match between the average posterior horizontal intrafacies K variogram and the model and average prior variogram is nearly perfect. The fact that the intrafacies conductivity distributions could be calibrated to the measurements without disturbing the prior geostatistics further illustrates that the calibrated lithology fields agreed with the measurements sufficiently well.

[59] Figures 11 and 12 show a performance test for the iterative postprocessing procedure, respectively for the bimodal and the trimodal field. From left to right, the number of K measurements is increased, and from top to bottom the number of head measurements is increased, both from 0 to 36. Thus the image in the upper left corner of Figures 11 and 12 shows the unconditional realization, while the image in the bottom right corner shows the maximally conditioned realization that is possible with the chosen measurement sets. Figures 11 and 12 illustrate that when both types of measurements are used together, they have a complementary effect. A quantification of this complementary effect is given in Figure 13, which shows how well the calibrated fields reproduce the reference lithology field. Comparing Figure 13a with Figure 13b reveals that, especially for head measurements, reproducing the reference lithology distribution requires much more sampling effort when the number of lithologies is larger. This can easily be explained from the increased number of possible lithology configurations that produce the same head responses at the measurement locations and still are conditional to the hard data. In the trimodal field (Figure 12), it takes the most extended conditioning set to capture most of the reference field characteristics. The poor resemblance, still, of the right hand quarter of the maximally conditioned field with the reference field is due to the small prior head variance in this area (dictated by the boundary conditions), indicating a small information content of the head measurements in that area.

[60] In Figure 13a it can be seen that a better reproduction of the true lithology distribution is achieved when using the 36H measurement set than when additional to this measurement set observations of K are incorporated in the calibration. The reason is that K measurements, depending on their location, can introduce a bias into the site characterization that is only corrected by head measurements for the part that is important for reproducing the head at the measurement locations. The opposite, a worse lithology reproduction when including more head measurements, can also happen (for instance when going from the

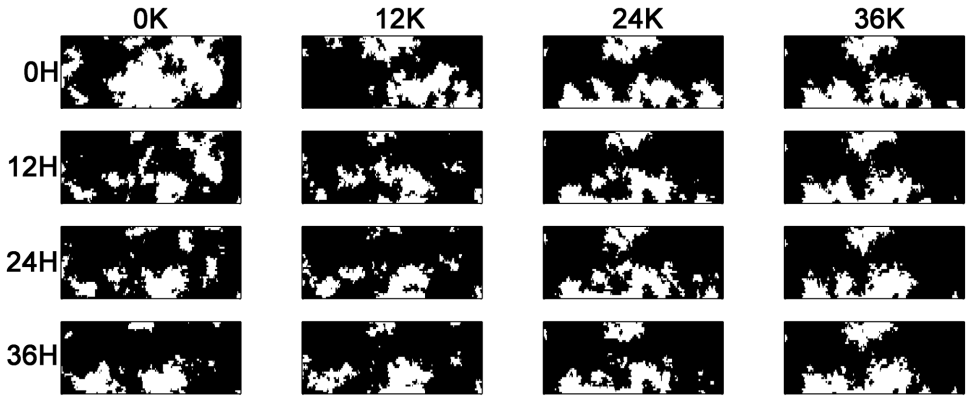

Figure 11. Performance test for the bimodal case. From left to right, the number of K measurements increases, and from top to bottom the number of head measurements increases.

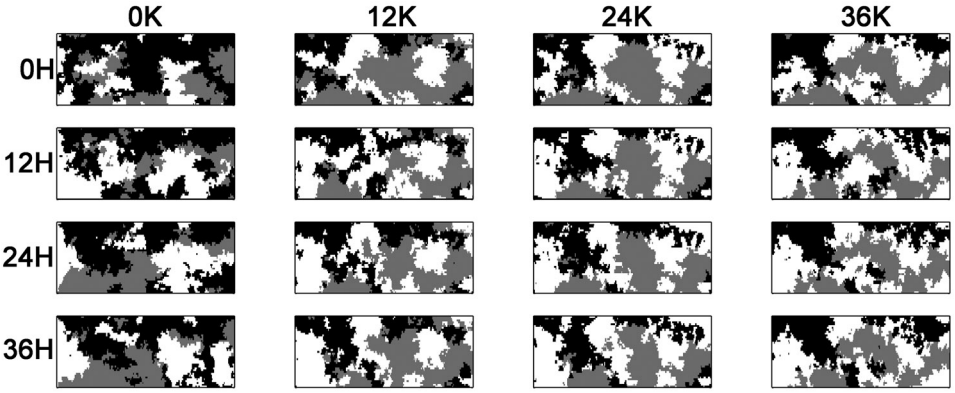

Figure 12. Performance test for the trimodal case.

12H24K to the 24H24K measurement set in Figure 13a). Depending on the location of the additional head measurements, the solution toward reproducing all measurements is not always found in lithology changes toward the reference lithology field. In other words, also head measurements can introduce a bias. Both phenomena make that a monotonically decreasing value of S_I (the number of cells in the posterior field not having the correct lithology) in Figure 13 is not guaranteed.

5. Discussion and Conclusions

[61] We proposed a method that can generate realizations of a continuous, multimodal hydraulic conductivity distribution, conditioned on both state measurements and static data. The geostatistical parameterization of the method is simple: it only requires prior estimates of the lithology ratios and variograms, prior estimates of the intralithology K statistics, and a variogram analysis on (a large number of) transformed fields. For calibrations that start with homogeneous prior fields, the method, when compared to the unimodal application of the representer algorithm, only involves (1) the replacement of the usual logarithmic transformation applied on the hydraulic conductivity data, (2) recalculation of the parameter covariance matrix for the transformed parameter, and (3) a back transformation procedure. For calibration of heterogeneous, multimodal prior fields, we proposed an iterative postprocessing procedure that ensures the preservation of the original geostatistics.

[62] In the example calculations, contrasts between the hydraulic conductivities of the various lithologies were large. In this situation, the intrafacies hydraulic conductivity distributions will only have a very minor influence on the flow and therefore their calibration (step 9 in the iterative postprocessing procedure) serves no practical purpose. We chose to use high-contrast examples to demonstrate the applicability of our method even when the problem is highly nonlinear and the derivative of K to α is locally very large, potentially causing numerical instability from equation (7). In our examples, this did not keep the calibration algorithm from finding realistic solutions to the inverse problem. For less contrasting lithologies and for wider intrafacies K distributions, problems from equation (7) are likely to be alleviated, so the method is readily applicable to these cases. It should be noted here that our methodology needs modification when applied to significantly overlapping intrafacies K distributions, as that case asks for a more involved translation procedure from K to lithology type.

[63] In the iterative postprocessing procedure, it was found necessary in step 2 to generate new intrafacies K distributions in every iteration, to avoid premature stagnation of the convergence and distortion of the geostatistics. So technically, the calibration of the lithology field and the calibration of the intrafacies K distributions are decoupled. In our examples this decoupling is justified, since the head field perturbation resulting from varying the intrafacies K realization ($\sigma^2_{head,\mathrm{m}}$) hardly ever (and in the trimodal example even never) exceeded the measurement error variance at the sampling locations. This implies that the head measurements did not contain any information on the intrafacies K distribution, but merely on the lithology distribution. Therefore it is irrelevant which intrafacies K realizations are used to perform the calibration of the lithology field. In cases where the head measurements *do* give information on the intrafacies K distributions (for example when the contrast in K between the different lithologies is smaller), a technically sound calibration of both the lithology field and the intralithology distributions rules out random replacement of the prior intrafacies realizations in step 2. This step should then be replaced by a perturbation of the prior intrafacies K realization, large enough to prevent premature convergence stagnation and geostatistical distortion, but small enough to keep the head perturbation at the sampling locations within the range explainable by the measurement error.

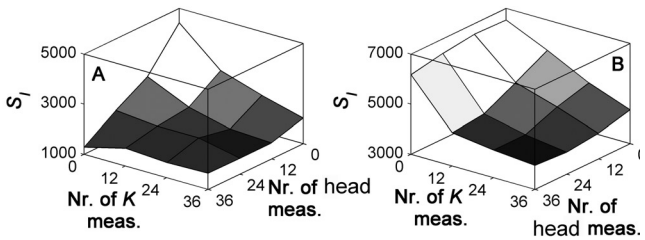

Figure 13. Quantification of the match between the reference field and the fields shown in (a) Figure 11 and (b) Figure 12. S_I is the number of cells with a lithology that is different from the lithology in the corresponding cell of the reference field.

[64] The required CPU time is the most important disadvantage of the proposed iterative postprocessing procedure. Using an Intel Pentium 4 2.4 GHz processor with 256 Mb internal memory, it took between 2 and 10 hours to calibrate one realization on 24 head measurements.

Appendix A: Inference of the Parameterization by Representers

[65] For easy reference, we provide a condensed derivation of the set of Euler-Lagrange equations and its solution. For a full derivation we refer to *Valstar* [2001] and *Valstar et al.* [2004].

[66] In the minimum of the objective function the variation of the objective function is zero for any variation of the random variables. Forcing this condition on equation (3) yields the Euler-Lagrange equations:

$$A_{gf}(\alpha)\lambda_f = \frac{\partial M_p(h)}{\partial h_g}\left[P_v^{-1}\right]_{pn}(z_n - M_n(h)) \tag{A1}$$

$$\alpha_l = \overline{\alpha_l} - P_{\alpha_{lk}}\left[h_g \frac{\partial A_{gf}(\alpha)}{\partial \alpha_k}\lambda_f\right] \tag{A2}$$

$$A_{gf}(\alpha)h_g = q_f, \tag{A3}$$

where f and g range from 1 to the number of head state variables; k and l range from 1 to the number of uncertain parameters; and n and p range from 1 to the number of measurements. Indices repeated within a single product term are assumed to be summed over appropriate ranges.

[67] The solution of the set of equations given by equations (A1), (A2), and (A3) minimizes the objective function. For this solution, an efficient parameterization with representers is applied. The definitions of the representer functions are

$$\lambda_f = \sum_{p=1}^{N_z} \Gamma_{fp} b_p \tag{A4}$$

$$\alpha_l = \overline{\alpha_l} + \sum_{p=1}^{N_z} \Psi_{lp} b_p \tag{A5}$$

$$h_g = h_{F_g} + h_{corr_g} + \sum_{p=1}^{N_z} \Xi_{gp} b_p, \tag{A6}$$

where b = the vector of representer coefficients, Γ_{fp} = the head adjoint representer for measurement p, calculated for head state variable f, Ψ_{lp} = the parameter representer for measurement p, calculated for uncertain parameter l, h_{F_g} = the prior estimates of the heads, Ξ_{gp} = the head representer for measurement p, calculated for head state variable g, h_{corr_g} = a head correction term, needed to fulfill the flow equation (as the head expansion is performed around the last estimates, whereas the parameters are expanded around their prior means), N_z = the number of measurements, and $\bar{\alpha}_l$ = the prior estimates of the parameters. Defining b as

$$b_p = \left[P_v^{-1}\right]_{np}\left(z_n - M_n\left(h_F + h_{corr} + \Xi_p\right)\right), \tag{A7}$$

and subsequently inserting the representer definitions in the Euler-Lagrange equations and dividing by equation (A7) yields explicit expressions for all representers and the correction term. These expressions still depend on the optimal estimates for the parameters and state variables, which are unknown initially and have to be found iteratively. During iteration η, the head adjoint representer Γ_{fp}^{η} is given by

$$A_{gf}\left(\hat{\alpha}^{\eta-1}\right)\Gamma_{fp}^{\eta} = \frac{\partial M_p\left(\hat{h}^{\eta-1}\right)}{\partial h_g}. \tag{A8}$$

The expression for the parameter representer Ψ_{lp}^{η} is

$$\Psi_{lp}^{\eta} = -P_{\alpha_{lk}}\left[\hat{h}_g^{\eta-1}\frac{\partial A_{gf}\left(\hat{\alpha}^{\eta-1}\right)}{\partial \alpha_k}\Gamma_{fp}^{\eta}\right]. \tag{A9}$$

The expression for the head representer Ξ_{gp}^{η} is

$$A_{fg}\left(\hat{\alpha}^{\eta-1}\right)\Xi_{gp}^{\eta} = -\frac{\partial A_{fg}\left(\hat{\alpha}^{\eta-1}\right)}{\partial \alpha_k}\Psi_{kp}^{\eta}\hat{h}_g^{\eta-1}. \tag{A10}$$

The expression for the head correction term h_{corr_g} is

$$A_{fg}\left(\hat{\alpha}^{\eta-1}\right)h_{corr_g} = q_f + \frac{\partial A_{fg}\left(\hat{\alpha}^{\eta-1}\right)}{\partial \alpha_k}\left(\hat{\alpha}_k^{\eta-1} - \overline{\alpha_k}\right)\hat{h}_g^{\eta-1} - A_{fg}\left(\hat{\alpha}^{\eta-1}\right)h_{F_g}. \tag{A11}$$

Finally, the representer coefficients b_p^{η} can be calculated by a rearrangement of equation (A7):

$$\left(\left[P_v\right]_{np} + M_n\left(\Xi_p^n\right)\right)b_p^n = \left(z_n - M_n\left(h_F + h_{corr}^{\eta}\right)\right), \tag{A12}$$

where $M_n(\Xi_p^{\eta})$ is the representer matrix, which consists of all representers at the locations of the measurements.

[68] The algorithm was assumed to have reached convergence when all differences between the measurement predictions from the representer expansion ($h_F + h_{corr} + \Xi b$) and the measurement predictions from the forward model with the updated parameters were smaller than a threshold value. For this research, this threshold value was set at 0.015 m.

[69] **Acknowledgments.** This research was partly funded by the Netherlands Institute of Applied Geosciences TNO–National Geological Survey. We would like to thank the three anonymous reviewers, whose comments and suggestions greatly improved this manuscript.

References

Bierkens, M. F. P. (1994), Complex confining layers: A stochastic analysis of hydraulic properties at various scales, Ph.D. thesis, Univ. of Utrecht, Utrecht, Netherlands.

Deutsch, C. V., and A. G. Journel (1998), *Geostatistical Software Library and User's Guide*, *Appl. Geostat. Ser.*, Oxford Univ. Press, New York.

Dowd, P. A., E. Pardo-Iguzquiza, and C. Xu (2003), Plurigau: A computer program for simulating spatial facies using the truncated plurigaussian method, *Comput. Geosci.*, *29*, 123–141.

Freeze, R. A. (1975), A stochastic-conceptual analysis of one-dimensional groundwater flow in non-uniform homogeneous media, *Water Resour. Res.*, *11*, 725–741.

Galli, A., H. Beucher, G. Le Lec'h, and B. Doligez (1994), The pros and cons of the truncated Gaussian method, in *Geostatistical Simulations*, edited by P.A. Dowd, pp. 217–233, Springer, New York.

Gomez-Hernandez, J. J., A. Sahuquillo, and J. E. Capilla (1998), Stochastic simulation of transmissivity fields conditional to both transmissivity and piezometric data: 1. Theory, *J. Hydrol.*, *203*, 162–174.

Hendricks Franssen, H. J. W. M., and J. J. Gomez-Hernandez (2002), 3D inverse modelling of groundwater flow at a fractured site using a stochastic continuum model with multiple statistical populations, *Stochastic Environ. Res. Risk Assess.*, *16*, 155–174.

Hoeksema, R. J., and P. K. Kitanidis (1985), Analysis of spatial structure of properties of selected aquifers, *Water Resour. Res.*, *21*, 563–572.

Hu, L. Y. (2000), Gradual deformation and iterative calibration of Gaussian-related stochastic models, *Math. Geol.*, *32*, 87–108.

Hu, L. Y., M. Le Ravalec, and G. Blanc (2001), Gradual deformation and iterative calibration of truncated Gaussian simulations, *Pet. Geosci.*, *7*, S25–S30.

Liu, N., and D. S. Oliver (2003), Conditional simulation of truncated random fields using gradient methods, paper presented at 2003 Meeting of the International Association for Mathematical Geology, Portsmouth, U. K.

Liu, N., and D. S. Oliver (2004), Automatic history matching of geologic facies, *SPE J.*, *9*(4), 429–436.

Lu, Z., and D. Zhang (2002), On stochastic modeling of flow in multimodal heterogeneous formations, *Water Resour. Res.*, *38*(10), 1190, doi:10.1029/2001WR001026.

McDonald, M. G., and A. W. Harbaugh (1984), A modular three-dimensional finite-difference ground-water flow model, *U.S. Geol. Surv. Open File Rep. 97–571*.

Pollock, D. W. (1994), User's guide for MODPATH/MODPATH-PLOT, version 3: A particle-tracking post-processing package for MODFLOW, the U.S. Geological Survey finite-difference ground-water flow model, *U.S. Geol. Surv. Open File Rep. 94–464*.

Press, W. H., B. P. Flannery, S. A. Teukolsky, and W. T. Vettering (1986), *Numerical Recipes: The Art of Scientific Computing*, Univ. of Cambridge Press, New York.

Rubin, Y. (1995), Flow and transport in bimodal heterogeneous formations, *Water Resour. Res.*, *31*, 2461–2468.

Rubin, Y. (2003), *Applied Stochastic Hydrogeology*, Oxford Univ. Press, New York.

Sun, N.-Z., M.-C. Jeng, and W. W.-G. Yeh (1995), A proposed geological parameterization method for parameter identification in three-dimensional groundwater modeling, *Water Resour. Res.*, *31*, 89–102.

Valstar, J. R. (2001), Inverse modeling of groundwater flow and transport, Ph.D. thesis, Delft Univ. of Technology, Delft, Netherlands.

Valstar, J. R., D. B. McLaughlin, C. B. M. Stroet, and F. C. van Geer (2004), A representer-based inverse method for groundwater flow and transport applications, *Water Resour. Res.*, *40*, W05116, doi:10.1029/2003WR002922.

Wen, X.-H., T. T. Tran, R. A. Behrens, and J. J. Gomez-Hernandez (2002), Production data integration in sand/shale reservoirs using sequential self-calibration and GeoMorphing: A comparison, *SPE Reservoir Eng. Eval. Eng.*, *5*, 255–265.

G. M. C. M. Janssen, Department of Soil Quality, Wageningen University, Dreijenplein 10, NL-6703 HB Wageningen, Netherlands. (gijs.janssen@wur.nl)

J. R. Valstar, Netherlands Institute of Applied Geosciences TNO–National Geological Survey, Princetonlaan 6, NL-3508 TA Utrecht, Netherlands.

S. E. A. T. M. van der Zee, Department of Ecohydrology, Wageningen University, Nieuwe Kanaal 11, NL-6706 PA Wageningen, Netherlands.